Research Square

Preprints are preliminary reports that have not undergone peer review.
They should not be considered conclusive, used to inform clinical practice,
or referenced by the media as validated information.

Effective Lorentz Factor and Analogue Horizon in a Giant Quantum Vortex of Superfluid Helium-4: Design of a Laboratory-Scale Pre- Experiment with an Optional Cryogenic Module for a Dual-Capsule Apparatus

Hasan Börekci

hborekci@hotmail.com.tr

HB ZECHMANN Medical Company

Research Article

Keywords: analogue gravity, superfluid helium-4, quantum vortex, effective Lorentz factor, analogue horizon, cryogenic design

Posted Date: September 29th, 2026

DOI: https://doi.org/10.21203/rs.3.rs-11187332/v1

License: This work is licensed under a Creative Commons Attribution 4.0 International License.
Read Full License

Additional Declarations: Competing interest reported. Financial interests: The author is the applicant of Turkish patent application TÜRKPATENT 2026/011037 concerning the dual-capsule (BEF) apparatus described in Sect. 3.10 of the manuscript; the laboratory-scale experiment (Stage 0) is independent of that application. The author has no other financial interests. Non-financial interests: none.

Effective Lorentz Factor and Analogue Horizon in a Giant Quantum Vortex of Superfluid Helium-4: Design of a Laboratory-Scale Pre-Experiment with an Optional Cryogenic Module for a Dual-Capsule Apparatus

Hasan Börekci

R&D Department, HB ZECHMANN Medical Company, Manisa Technopark, Manisa, Türkiye

(independent researcher; not employed by any state-affiliated institution)

Corresponding author: hborekci@hotmail.com.tr · ORCID 0000-0001-9137-6342

Acknowledgements

The author received no institutional support for the design or writing of this work, is not employed by any state-affiliated institution, and carried out the work with his own means. The conception, planning and apparatus design are the author's own. Large-language-model tools were used for the literature search, for checking the calculations and for page layout, as documented in Sect. 3.12; all scientific content and the final text are the author's responsibility. The basic layout of the vortex cell is adapted from the published apparatus of Švančara et al. (Nature 628, 66, 2024).

Abstract

A laboratory-scale pre-experiment is designed in which a stable giant quantum vortex in superfluid helium-4 produces, for the surface waves of the liquid, an effective Lorentz factor $\gamma_{eff} = (1 - v^2/c_w^2)^{-1/2}$, where v is the flow speed and c_w the wave speed. For bulk sound the Landau critical velocity (≈58.8 m/s) limits γ_{eff} to 1.032, whereas capillary–gravity surface waves have a minimum phase speed of ≈9.89 cm/s, so that an analogue ergoregion and horizon form. For a draining vortex carrying $N = 4\times10^4$ circulation quanta in a 40 mm deep cell the ergoregion radius is 6.70 mm, the analogue-horizon radius 1.92 mm and the hollow-core radius 0.75 mm; γ_{eff} reaches 1.67 at $r = 1.25\ r_e$ and 3.28 at $r = 1.05\ r_e$. The cryostat, helium supply, purification, pumping and recovery system, flow loop, metrology and protocol are specified in detail; every design number is traceable to an open calculation model. The effective factor applies only to waves in the helium; it is not a real time dilation for clocks or living organisms. Optional installation of the module in the inner capsule of the author's dual-capsule apparatus (Stage 1) is analysed: standard general relativity predicts no measurable ON/OFF difference, and the attainable bound on the phenomenological parameter ξ (≈10^{35}–10^{43}) is weaker than existing clock bounds. Finally, the node-spacing function of the author's Börekci-2 metric is shown to equal the inverse effective Lorentz factor of the Painlevé–Gullstrand river flow, a known property re-expressed in analogue-gravity language.

Keywords: analogue gravity; superfluid helium-4; quantum vortex; effective Lorentz factor; analogue horizon; cryogenic design

1 Introduction

Unruh [1] showed that sound waves in a moving fluid obey the same equations as fields propagating in a curved spacetime, founding the field of analogue gravity. Visser [2] showed that the analogy includes horizons and ergoregions, and Barceló, Liberati and Visser [3] reviewed the field. Experimentally, analogue Hawking radiation and its entanglement [4] and thermal Hawking radiation with its temperature [5] were observed in Bose–Einstein condensates; rotational superradiance [6] and quasinormal-mode oscillations [7] were measured in water vortices, and the associated spectroscopy was formalised in [8].

Superfluid helium occupies a special place among these platforms. The fluid–gravity analogy requires vanishing viscosity, which is realised naturally in liquid helium and in cold atomic clouds [9]. Owing to the large zero-point motion and weak attraction of its atoms, helium is the only substance that remains liquid down to absolute zero at pressures below about 25 bar;

hydrogen, although lighter, solidifies at ≈14 K. Molecules embedded in superfluid helium droplets rotate freely, as in vacuum [10], illustrating the "vacuum-like" behaviour of this medium. Room-temperature helium gas is therefore unsuitable for the present purpose; the required medium is superfluid liquid helium below 2.17 K. Švančara et al. [9] stabilised a giant vortex carrying thousands of circulation quanta in superfluid ^{4}He and observed bound states and analogue black-hole ringdown signatures in the surface waves. The same group has since reported black-hole spectroscopy with several quasinormal modes extracted from the same platform [11], the origin of quasinormal modes in semi-open systems [12], a digital holographic method for imaging the free surface of superfluid helium [13] and, in September 2026, a laboratory realisation of the black-hole-bomb instability in a draining He II vortex, in which about 1.2×10^5 circulation quanta are reported to contribute to the central vortex [14]. Desrochers, Marchand and Stamp [15] modelled the vacuum tunnelling of vortex pairs in thin He II films as an analogue of the Schwinger effect and proposed an experiment to test it.

This work answers a question raised within the author's BEF (Börekci Energy Field) programme [16]: if superfluid helium were placed in the inner capsule of that apparatus, could an effective Lorentz factor be produced? The answer has two layers, and this dual framing is kept throughout: (i) an effective Lorentz factor for the waves in the helium can be produced and measured; (ii) this factor is not a real time dilation for the atoms, clocks or a living subject inside the capsule. The aims are to compute the accessible γ_{eff}, to design an independent laboratory pre-experiment (Stage 0) in sufficient detail to be built, to assess honestly its integration into the inner capsule (Stage 1), and to relate the result to the author's black-hole-matter hypothesis [17].

2 Theoretical framework

2.1 Acoustic (analogue) metric

Small perturbations in an inviscid, irrotational fluid "see" the effective metric determined by the local wave speed c and flow velocity $\mathbf{v}$ [1, 2]:

$$\mathrm{d}s^2 = (\rho/c)\,[\,-(c^2 - v^2)\,\mathrm{d}t^2 - 2\,\mathbf{v}\cdot\mathrm{d}\mathbf{x}\,\mathrm{d}t + \mathrm{d}\mathbf{x}\cdot\mathrm{d}\mathbf{x}\,] \qquad (1)$$

The wave speed c replaces the speed of light. The region where the flow exceeds the wave speed is the ergoregion; the surface where the radial flow exceeds the wave speed is the analogue horizon.

2.2 Effective Lorentz factor

Two kinds of observer can be read from metric (1). For a point moving with the fluid, $d\tau \propto dt$: there is no analogue time dilation. For a point fixed in the laboratory past which the fluid flows at speed v (for example a detector), $d\tau \propto \sqrt{(1 - v^2/c^2)}\, dt$. The kinematic factor of motion relative to the medium is therefore the formal counterpart of the special-relativistic Lorentz factor:

$$\gamma_{\mathrm{eff}} = 1 / \sqrt{(1 - \beta^2)}, \quad \beta = v / c_w \tag{2}$$

This is the analogue of the $\sqrt{(1 - r_s/r)}$ time-dilation factor of a static observer in Schwarzschild spacetime (Sect. 2.7). In the limit $\beta \to 1$, γ_{eff} diverges: a laboratory-static observer is no longer possible there. That surface is the ergoregion boundary; it coincides with the analogue horizon only when the flow is purely radial.

2.3 Bulk sound: the Landau limit

In He II the first-sound velocity is $c_1 \approx 237$ m/s [18]. Superflow cannot exceed the Landau critical velocity at which rotons are created:

$$v_L = \Delta / p_0 \approx 58.8\ \mathrm{m/s}, \quad \beta_{\max} = v_L/c_1 = 0.248, \quad \gamma_{\mathrm{eff,max}} = 1.032 \tag{3}$$

where $\Delta/k_B \approx 8.62$ K is the roton gap and $p_0/\hbar \approx 1.92$ Å^{-1} the roton momentum. The breakdown of superfluidity has been tested experimentally against Landau's theory [19]. The conclusion is clear: for bulk sound the largest attainable effective Lorentz factor is ≈1.032, so the main channel of the experiment is surface waves.

2.4 Surface waves and the minimum phase speed

The phase speed of capillary–gravity waves on deep liquid depends on the wavenumber k (dispersion):

$$c(k) = \sqrt{(\, g/k + \sigma k/\rho\,)}, \quad k_* = \sqrt{(\rho g/\sigma)}, \quad c_{\min} = (4g\sigma/\rho)^{1/4} \tag{4}$$

With $\rho \approx 145$ kg/m³ [18] and the zero-temperature surface tension $\sigma \approx 3.54\times10^{-4}$ N/m [20, 18] one obtains $k_* \approx 2005$ m^{-1}, $\lambda_* \approx 3.13$ mm, $c_{\min} = c_w \approx 9.89$ cm/s and $f_* \approx 31.6$ Hz. At the minimum phase speed the group velocity equals the phase velocity, so the dispersion is locally flat and the effective-metric description is best justified there [21]. The measurement waves are therefore chosen near $\lambda_* \approx 3.13$ mm. Two remarks on σ are needed. First, σ decreases with temperature: the adopted database of Donnelly and Barenghi [18] gives $\approx 3.3\times10^{-4}$ N/m at 1.6 K, i.e. about 7 % below the $T \to 0$ value; since $c_w \propto \sigma^{1/4}$ and $\lambda_* \propto \sigma^{1/2}$, this lowers c_w by ≈2 % (to ≈9.72 cm/s) and λ_* by ≈4 % (to ≈3.03 mm), and raises r_e by ≈2 % (to ≈6.82 mm). Second, an independent capillary-wave determination [22] gave 3.75×10^{-4} N/m, 6 % above the value adopted here; the corresponding uncertainty in c_w is 1.5 %. Neither effect changes the

conclusions, and the static calibration of Sect. 4.3 measures c_w and $\lambda*$ directly. Because the flow only needs to exceed ≈10 cm/s, the ergoregion and the horizon are produced at speeds far below the Landau limit.

2.5 Draining vortex: ergoregion and analogue horizon

For a vortex drained at its centre ("draining bathtub") the velocity field is

$$\mathbf{v} = -(D/r)\,\hat{\mathbf{r}} + (C/r)\,\hat{\boldsymbol{\theta}}, \quad C = \Gamma/2\pi, \quad \Gamma = N\,\kappa, \quad \kappa = h/m_4 \tag{5}$$

where $\kappa = 9.97\times10^{-8}$ m²/s is the circulation quantum of helium-4 and N the number of quanta carried by the vortex. The ergoregion (total speed > c_w) and analogue-horizon (radial speed > c_w) radii are [2]

$$r_e = \sqrt{(C^2 + D^2)} \,/\, c_w, \quad r_h = |D| \,/\, c_w \tag{6}$$

so that the radial profile of the effective Lorentz factor is

$$\gamma_{eff}(r) = [\,1 - (r_e/r)^2\,]^{-1/2}, \quad r > r_e \tag{7}$$

Bernoulli's relation gives the funnel shape of the free surface and the radius of the hollow core:

$$z(r) = h_0 - (C^2 + D^2) \,/\, (2\,g\,r^2), \quad r_{core} = \sqrt{(C^2 + D^2)} \,/\, \sqrt{(2\,g\,h_0)} \tag{8}$$

The ergoregion must be larger than the measurement wavelength ($r_e \geq \lambda*$), otherwise the waves cannot resolve it. For the design ratio D/C = 0.3 this requires at least

$$N \geq 2\pi\, c_w\, \lambda* \,/\, (\,\kappa\,\sqrt{(1 + (D/C)^2)}\,) \approx 1.87\times10^4 \tag{9}$$

The design value is $N = 4\times10^4$ ($\Gamma = 3.99\times10^{-3}$ m²/s). Švančara et al. [9] reported "thousands" of quanta, and the September 2026 preprint of the same group [14] reports about 1.2×10^5 quanta contributing to the central vortex of a draining flow; the design target therefore lies between the two published figures, and the associated risk is discussed in Sect. 9. Related theoretical and experimental studies of draining superfluid vortices are given in [23, 24, 25].

2.6 Distinction between effective and real time dilation

The γ_{eff} of Eq. (2) applies only to the helium's own waves. Atomic clocks, biochemical processes and a living subject operate through electromagnetic interactions whose "speed limit" is the real speed of light c, relative to which the helium flow is entirely negligible. Real time dilation is fixed by the real metric alone. The mass of helium in the cell (V = 1.26 L, M = 0.18 kg) produces at the cell scale a potential of only $\Phi/c^2 \approx 1.4\times10^{-27}$. This value is static and cancels in every ON/OFF comparison.

2.7 River model and the Börekci-2 metric

In Painlevé–Gullstrand coordinates the Schwarzschild spacetime can be written as a "river" of space flowing into the black hole at the escape velocity [26]:

$$ds^2 = -c^2\,dt^2 + (dr + v\,dt)^2 + r^2\,d\Omega^2, \quad v(r) = c\sqrt{(r_s/r)} \tag{10}$$

This has the same form as an acoustic metric with constant c. The effective Lorentz factor of the river gives

$$1 - v^2/c^2 = 1 - r_s/r = n_e{}^2(r) \quad \Longrightarrow \quad n_e(r) = 1 \,/\, \gamma_{\mathrm{eff,river}}(r) \tag{11}$$

where $n_e(r) = \sqrt{(1 - r_s/r)}$ is the node-spacing function of the Börekci-2 metric [17]. In the language of that hypothesis the contraction ratio of the node spacing equals the inverse effective Lorentz factor of the inflowing "river of space". Because $\gamma_{\mathrm{eff}}(r)$ in the helium experiment is fixed by the measured flow profile v(r), the experiment offers a laboratory counterpart of this relation for waves. Two limits must be stated: in the two-dimensional draining vortex $v \propto 1/r$ whereas in the Schwarzschild river $v \propto r^{-1/2}$; and for constant-density flow the continuity condition prevents an exact Schwarzschild mapping [2]. The experiment therefore produces an analogue of the same mathematical structure, not a copy of $n_e(r)$.

3 Materials and methods

3.1 Design overview and philosophy

The Stage 0 apparatus is a helium-bath cryostat containing a closed He II flow loop that sustains a stationary draining vortex in a cylindrical cell, with optical access from above and from the side for surface-wave metrology. All design values are engineering choices of the author, chosen so that (i) the ergoregion is resolved by the measurement waves (Eq. 9), (ii) the heat load is compatible with continuous operation at ≈1.6 K for at least 24 h from one liquid-helium fill, and (iii) every component can be procured or machined with standard low-temperature laboratory techniques [27]. Every number in this section is either a stated design choice or a quantity computed from it by the open calculation model (Sect. 3.12); none is a measured value. The apparatus is shown in isometric and side views in Figs. 1 and 2, the helium gas-handling and cryogenic circuit in Fig. 3 and the top view in Fig. 4; the part numbers are identical in Figs. 1, 2, 4 and 5.

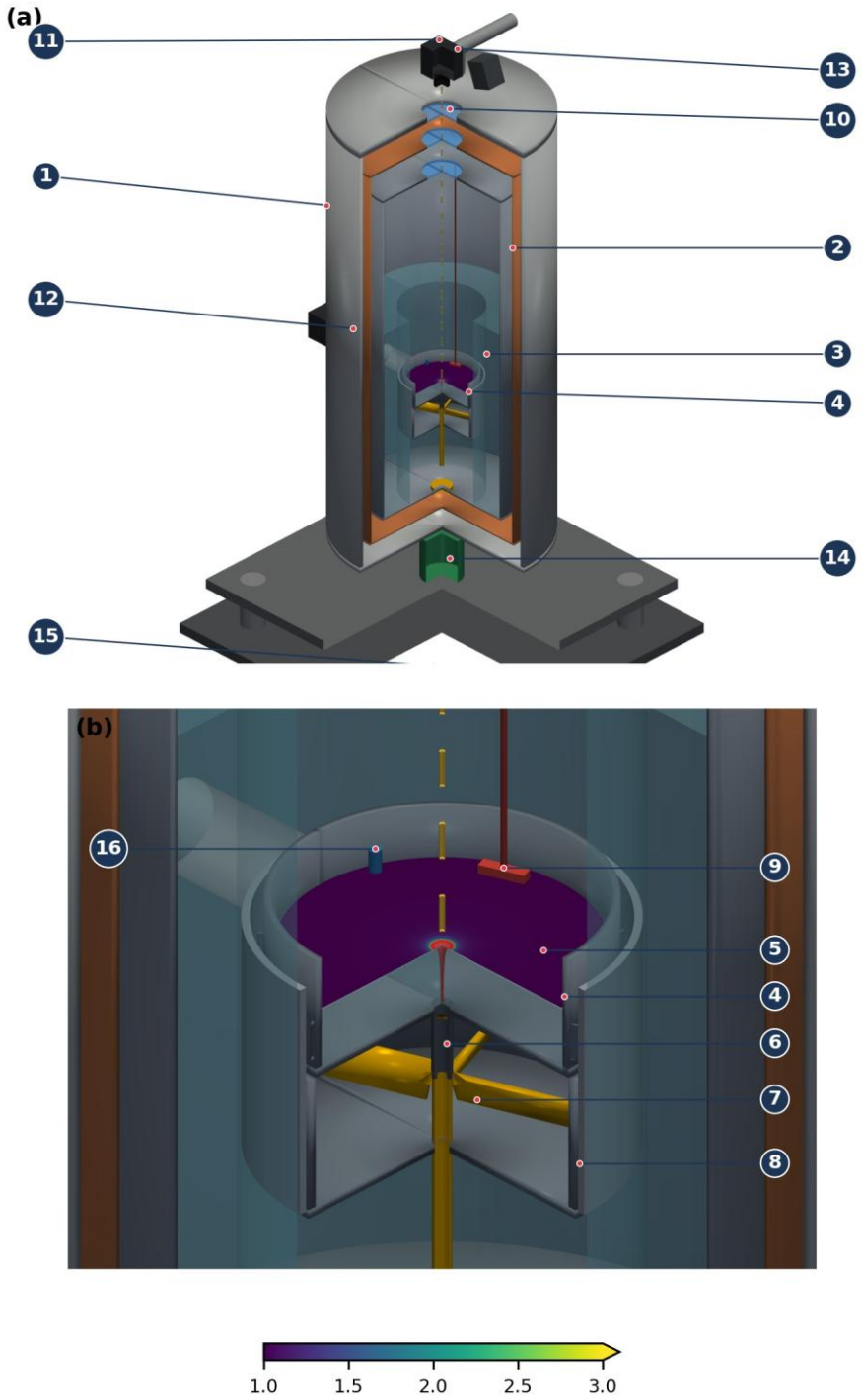


Fig. 1 (Color online) Isometric three-dimensional quarter-section view of the Stage 0 apparatus. (a) Complete cryostat with the front-right quarter removed to expose the layers. (b) Enlargement of the vortex cell; the colour of the free surface encodes γ_{eff} for surface waves and the red centre marks the ergoregion. Numbered parts (identical in Figs. 1, 2 and 4): 1 outer vacuum chamber (stainless steel, 300 K); 2 vapour-cooled copper radiation shield (≈50–80 K); 3 He II bath (vapour-pumped, ≈1.6 K); 4 vortex cell (200 mm inner diameter, 40 mm liquid depth); 5 free surface with vortex funnel (colour: γ_{eff}); 6 central drain tube (10 mm inner diameter); 7 propeller chamber, shaft and four-blade propeller; 8 return channel with twelve tangential inlet vanes; 9 wave generator (piezoelectric paddle, ≈32 Hz); 10 sapphire windows on the upper optical axis; 11 high-speed camera and fringe projector (Fourier-transform profilometry); 12 side observation window and shadowgraph camera; 13 vapour pumping line (to 1.6 K); 14 magnetically coupled propeller drive (motor at 300 K); 15 vibration-isolation platform (spring isolators); 16 RuO_2 thermometer and capacitive level sensor

3.2 Cryostat

The cryostat (parts 1–3, 13 in Figs. 1, 2 and 4) is a conventional helium-bath design. The outer vacuum chamber (part 1) is a 304L stainless-steel cylinder of 600 mm inner diameter and 1.3 m height, evacuated to below 10^{-5} mbar before cool-down by a turbomolecular pump and afterwards held by cryopumping. Inside it hangs a copper radiation shield (part 2) of 540 mm diameter, wrapped in 30 layers of multilayer insulation and cooled by the cold helium boil-off vapour flowing through its neck heat exchanger, which brings it to ≈50–80 K; a liquid-nitrogen jacket at 77 K is an acceptable alternative if a larger static heat load is accepted. The He II bath tank (part 3) is a 340 mm inner-diameter, 550 mm tall stainless-steel vessel holding ≈41 L of liquid at 4.2 K when full; it is suspended from the top plate by three thin-walled stainless-steel tubes that also serve as the fill, pumping and wiring ports. The vortex cell and its flow loop (Sect. 3.5) sit fully immersed in the bath, so that the whole loop is at the bath temperature and the cell walls are isothermal.

Optical access is provided along the vertical axis by three coaxial windows: a borosilicate window in the room-temperature top flange, an aperture with an infrared-blocking cold filter in the shield, and a 100 mm sapphire window (part 10) in the bath-tank lid directly above the cell. A second, horizontal line of sight through a 20 mm sapphire side window (part 12) at the height of the liquid surface allows shadowgraph imaging of the funnel profile. Windows are the dominant radiative heat path; the cold filter and the small side aperture keep this contribution below ≈20 mW in the design budget of Sect. 3.4.

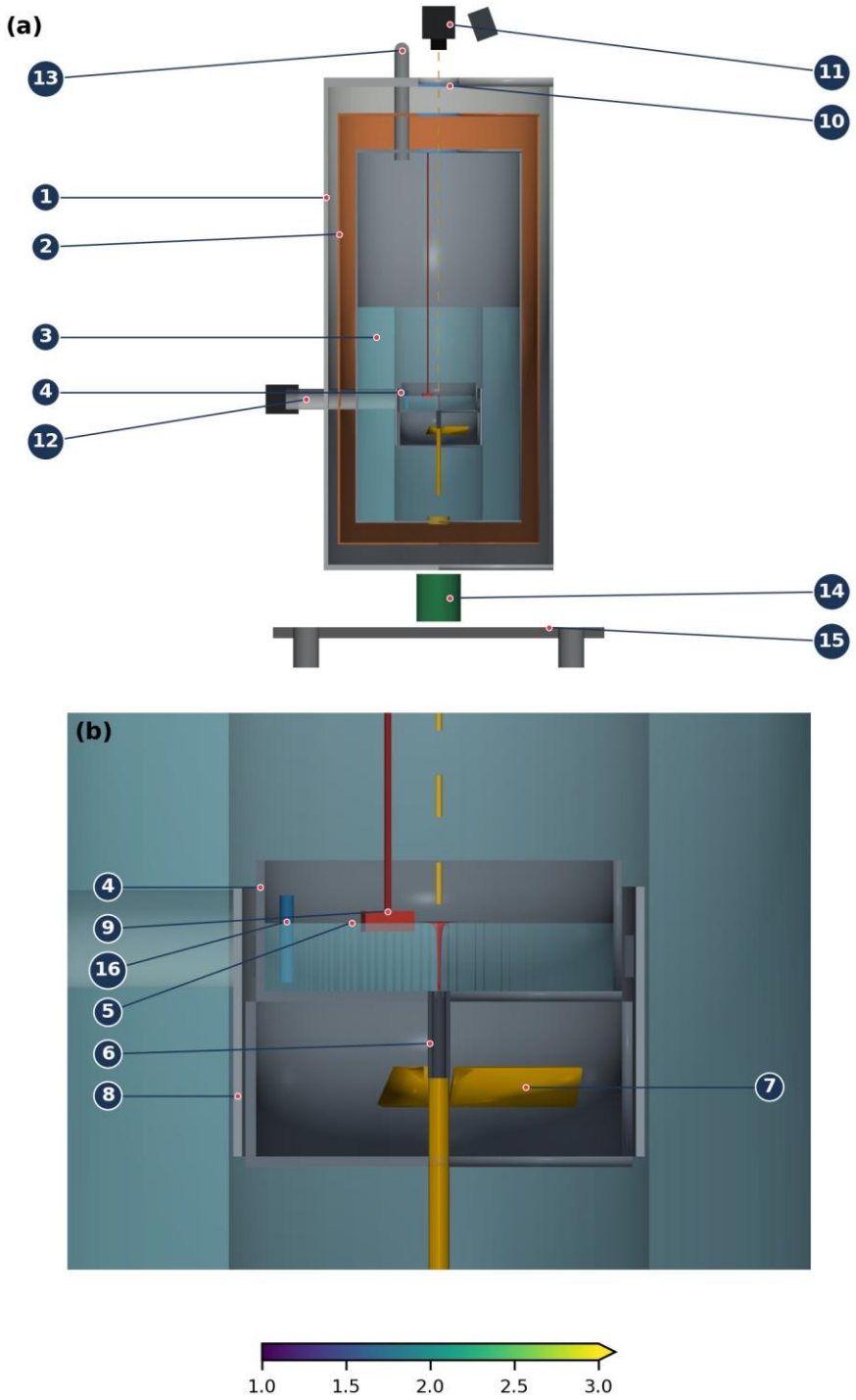


Fig. 2 (Color online) Side three-dimensional half-section of the Stage 0 apparatus (xz plane). (a) Cooling layers and the vertical optical axis. (b) Enlargement of the closed flow loop: propeller (7) → return channel (8) → cell (4) → vortex (5) → drain (6) → propeller. The red pointed funnel at the centre is the hollow vortex core. Part numbers as in Fig. 1

3.3 Helium supply, purification and gas-handling system

Figure 3a shows the helium circuit of Stage 0. Helium gas of 99.999 % purity (grade 5.0) is supplied from 50 L cylinders at 200 bar and passed through a liquid-nitrogen-cooled activated-charcoal trap that removes residual air, water and hydrocarbons, which would otherwise freeze in the transfer line or in the pumping line. Liquid helium at 4.2 K is delivered from a 100 L

transport dewar through a vacuum-insulated transfer line into the bath tank; a full fill of ≈41 L corresponds to ≈5.1 kg of helium, i.e. ≈29 m³ of gas at standard conditions, and this inventory is recovered rather than lost. The boil-off and the pumped vapour are collected in a gas bag, compressed to 200 bar into storage cylinders and returned through the purifier for the next fill (dashed line in Fig. 3a). All closed volumes carry spring-loaded relief valves and a burst disc rated well below the pressure that the vessel can withstand, and the laboratory is fitted with oxygen-deficiency monitors, because one litre of liquid helium expands to about 750 L of gas at room temperature.

Every helium-carrying joint is leak-tested with a helium mass-spectrometer leak detector to better than 10^{-9} mbar L/s at room temperature before cool-down; indium seals are used on all cryogenic flanges and on the sapphire windows. The cell, the flow loop and the bath tank are pumped and flushed with pure helium three times before the first transfer, so that no air remains to freeze at the drain orifice.

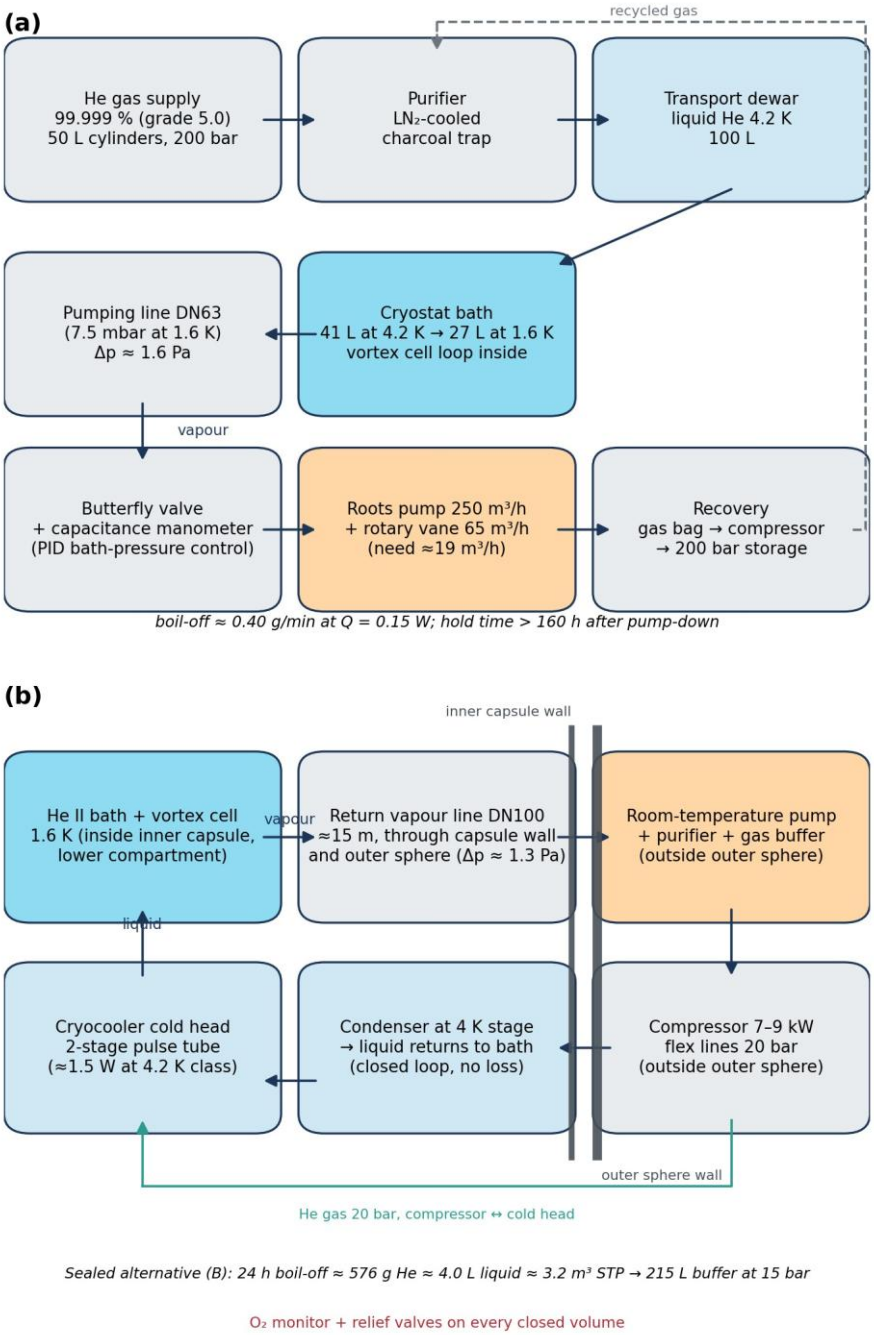


Fig. 3 (Color online) Helium gas-handling and cryogenic circuit. (a) Stage 0 open cycle with recovery: gas supply, purifier, transport dewar, cryostat bath, DN63 pumping line, pressure-regulating butterfly valve, Roots and rotary-vane pumps and the recovery loop (dashed); the line below the diagram gives the design boil-off and hold time. (b) Stage 1 closed-loop recondensing circuit (Option A) inside the dual-capsule apparatus: bath and vortex cell in the lower compartment of the inner capsule, DN100 vapour-return line through the inner-capsule wall and the outer sphere, room-temperature pump and buffer, and a pulse-tube cryocooler whose 4 K stage condenses the returned gas; the sealed alternative (Option B) is summarised below the diagram. All values are design numbers from the calculation model

3.4 Cooling to 1.6 K, vapour pumping and heat budget

After the transfer the bath is at 4.2 K. It is then cooled below the λ point (2.17 K) by pumping on its own vapour through the DN63 pumping line (part 13): the saturated vapour pressure of ^{4}He at 1.6 K is ≈7.5 mbar [18], and the latent heat of vaporisation there is ≈91 J/mol (≈22 J/g) [18]. Evaporative cooling from 4.2 K to 1.6 K consumes roughly 35 % of the liquid, leaving ≈27 L. The pumping system is a Roots blower of 250 m³/h backed by a rotary-vane pump of 65 m³/h; the bath pressure, and hence the temperature, is regulated by a motorised butterfly valve in the line, controlled by a PID loop on a capacitance manometer (10 mbar full scale) mounted at the room-temperature end of the line. Temperature is thus set through the ITS-90 helium vapour-pressure scale and cross-checked with the RuO_2 thermometers (Sect. 3.7).

The design heat-load budget for the bath at 1.6 K is Q = 0.15 W, allocated as ≈50 mW conduction and radiation through supports, wiring and the pumping line, ≈20 mW through the windows, ≈50 mW for the propeller drive (Sect. 3.5) and ≈30 mW of margin. The resulting boil-off is

$$\dot{m} = Q / L_{vap} \approx 6.7\ \mathrm{mg/s} \approx 0.40\ \mathrm{g/min}, \quad \text{corresponding to} \approx 0.17\ \mathrm{L/h\ of\ liquid} \tag{14}$$

so that one fill supports more than 160 h of operation at 1.6 K. At the pump inlet (293 K) this mass flow is a throughput of ≈4.1 Pa·m³/s, which at 7.5 mbar requires a volumetric pumping speed of only ≈19 m³/h; the pumps are oversized by an order of magnitude so that the initial pump-down from 4.2 K is fast. The viscous-flow conductance of a 3 m, 63 mm line at the mean line pressure is ≈2.5 m³/s, giving a pressure drop of only ≈1.6 Pa (Eq. 15):

$$C_{line} = \pi\, d^4\, \bar{p} / (128\, \eta\, L), \quad \Delta p = Q_{throughput} / C_{line} \tag{15}$$

with $\eta = 1.96\times10^{-5}$ Pa·s the viscosity of helium gas at 293 K. Bath pressure fluctuations produced by the pumps are recorded continuously (Sect. 7) because they modulate the surface tension and the liquid level.

3.5 Vortex cell and flow loop

The cell (part 4) is a cylinder of 200 mm inner diameter machined from oxygen-free copper and gold plated to avoid oxide layers; its floor is flat and its walls are polished to reduce nucleation of parasitic vortices. The design liquid depth is h_0 = 40 mm, more than ten times the measurement wavelength, so that the deep-liquid dispersion of Eq. (4) applies away from the funnel. The flow loop is the one of Švančara et al. [9] in its basic layout: a four-blade propeller of 60 mm diameter in a chamber below the cell (part 7) pushes liquid up an annular return channel around the cell (part 8); at the top of the channel twelve inlet vanes inject the liquid

tangentially into the cell, and the liquid leaves through the central drain tube (part 6) of 10 mm inner diameter back into the propeller chamber. The vane angle fixes the ratio of radial to azimuthal inflow; for the design ratio D/C = 0.3 the vanes are set at arctan(0.3) ≈ 17° from the tangent. In the ideal two-dimensional model the loop must circulate $Q \approx 2\pi\, D\, h_0 \approx 48$ mL/s, which at this depth corresponds to a mean drain velocity of a few centimetres per second; the ideal hydraulic power $\rho\, g\, \Delta h\, Q$ for a head of 5 cm is only ≈3.4 mW.

The propeller is driven without any rotating vacuum seal at the bath: the bath-tank floor carries a thin-walled (1 mm) stainless-steel re-entrant cup; inside the cup, in the insulating vacuum, sits a driving rotor with permanent magnets, and the propeller shaft carries the driven magnet ring inside the bath. The driving rotor is thermally anchored to the radiation shield by a flexible copper braid, so that it radiates at shield temperature rather than at 300 K, and it is turned through a thin-walled stainless-steel shaft by a motor mounted at room temperature under the cryostat (part 14). At the design speed of about one revolution per second the eddy-current heating in the 1 mm stainless cup is at the milliwatt level (≈3.7 mW for a 0.3 T coupling field, Eq. 16), and the conduction along the shaft is intercepted at the shield; the 50 mW allocated to the drive in Sect. 3.4 is therefore a conservative envelope:

$$P_{\mathrm{eddy}} \approx (\sigma_e\, E^2\, V_{\mathrm{cup}}), \quad E \approx \omega\, a\, B\, /\, 2 \tag{16}$$

where $\sigma_e \approx 1.4\times10^6$ S/m is the low-temperature conductivity of stainless steel, ω the angular velocity, a the cup radius and V_{cup} the volume of the cup wall. The propeller speed is ramped in steps by the motor controller and the circulation Γ is not assumed but measured from the azimuthal velocity profile (Sect. 4).

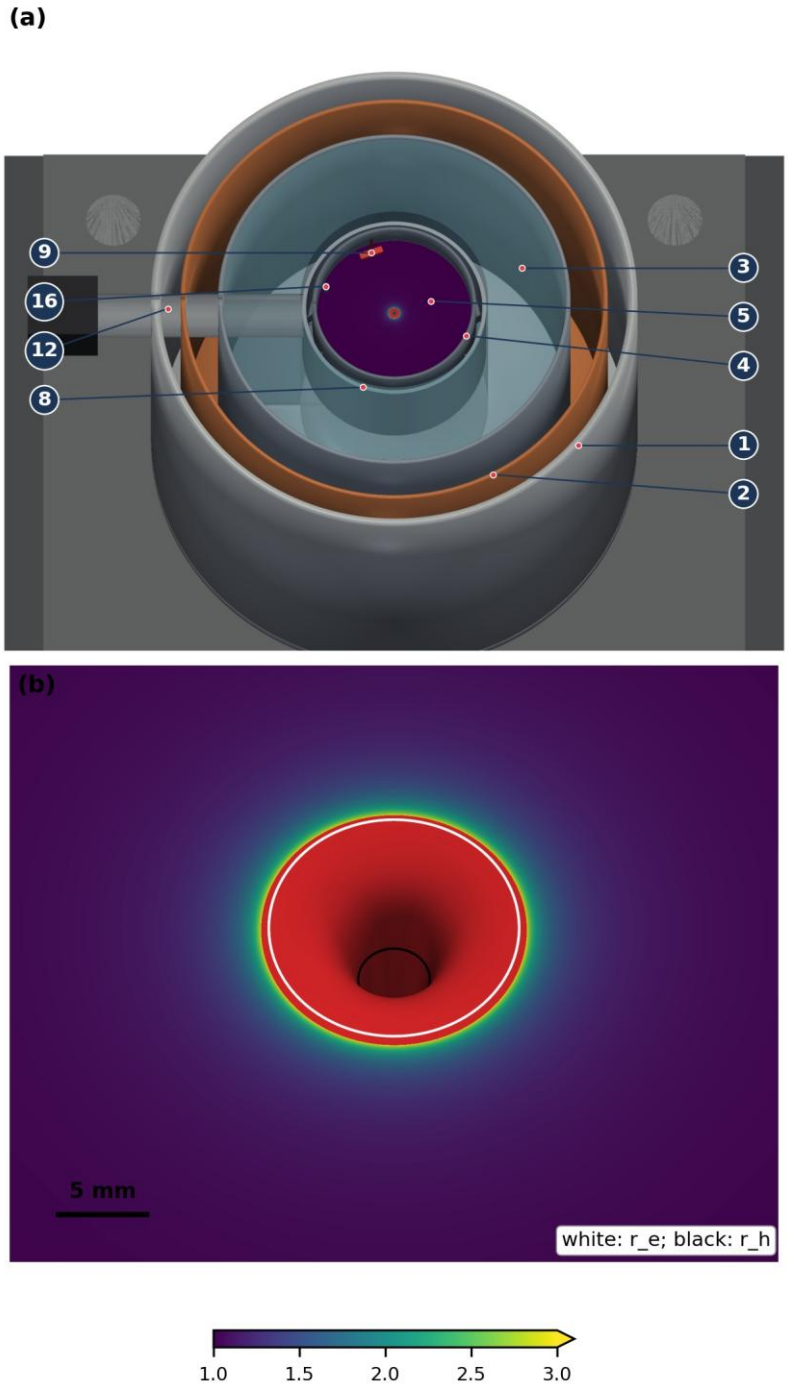


Fig. 4 (Color online) Top three-dimensional view. (a) Horizontal section 90 mm above the cell floor, viewed 20° from the vertical. (b) Three-dimensional view of the vortex centre, 30° from the vertical, field of view ≈ ±16 mm, with a 5 mm scale bar: the white circle marks the ergoregion boundary (r_e = 6.70 mm) and the black circle the analogue horizon (r_h = 1.92 mm). The colour scale is γ_{eff}; in the red region the flow exceeds the wave speed. Part numbers as in Fig. 1

3.6 Wave excitation and surface-wave metrology

Surface waves are excited by a piezoelectric paddle (part 9) mounted at the cell wall and driven by a function generator; the drive frequency is scanned between 10 and 100 Hz for the dispersion calibration and set near $f_* \approx 31.6$ Hz ($\lambda_* \approx 3.13$ mm) for the mapping runs, with

amplitudes of 10–50 μm so that the waves remain linear. Short wave packets (three to five cycles) are used for the ringdown measurements of Sect. 4.2. The free-surface height field η(x, y, t) is measured through the top window by Fourier-transform profilometry [28]: a sinusoidal fringe pattern is projected obliquely onto the surface by an LED projector (part 11) and imaged by a high-speed camera (2048 × 2048 pixels, 500 frames per second, i.e. 16 frames per period at f∗), covering a field of view of 60 mm × 60 mm at ≈30 μm per pixel; the phase of the deformed fringes gives η with micrometre-level height resolution after unwrapping. Two alternatives used in the analogue-gravity community can be substituted without changing the analysis: fast checkerboard demodulation [29] and digital holographic imaging of the superfluid surface [13]. The side window (part 12) provides a shadowgraph of the funnel and a direct, model-independent measurement of the hollow-core radius.

3.7 Thermometry, level, pressure and control

Temperature is measured by two calibrated ruthenium-oxide resistance thermometers (part 16), one in the bath and one in the cell wall, read by a four-wire AC resistance bridge; the bath vapour pressure gives an independent temperature through the vapour-pressure scale. A capacitive level sensor in the bath and a second one in the cell monitor the liquid heights; the cell level is kept at $h_0 = 40$ mm by the loop itself, whose return flow is limited by an overflow weir at the top of the return channel. A 0–1 W resistive heater in the bath allows controlled temperature scans between 1.4 and 2.1 K to study the damping of the surface waves as a function of the normal-fluid fraction. All sensors, the motor controller, the wave generator and the camera trigger are synchronised by a common data-acquisition clock so that every image is tagged with the instantaneous temperature, pressure, level and propeller speed.

3.8 Vibration and acoustic isolation

Micrometre-level surface metrology is vulnerable to vibration. The cryostat stands on a passive vibration-isolation platform (part 15) with spring isolators of ≈1.5 Hz natural frequency; the pumps are placed in an adjacent room on their own foundation and connected to the pumping line through two flexible bellows sections and a heavy inertial block; the camera and projector are mounted on the same isolated platform as the cryostat so that they share its motion. Three-axis accelerometers on the cryostat top plate and on the pump line, and a microphone in the laboratory, are recorded synchronously with every run and are used as veto channels in the analysis (Sect. 7).

3.9 Data analysis pipeline

The analysis follows the procedure of the water-vortex and helium-vortex experiments [6, 7, 9]: (i) $\eta(x, y, t)$ is reconstructed from the fringe images; (ii) it is resampled onto polar coordinates centred on the vortex axis, which is located from the shadowgraph; (iii) for each radius a two-dimensional Fourier transform in azimuthal angle and time gives the dispersion $\omega(m)$ of co- and counter-rotating waves, from which c_+ and c_- and hence $v_\theta(r)$ and c_w follow by Eq. (12); (iv) the same is done in the radial direction for $v_r(r)$; (v) $\gamma_{eff}(r)$, r_e and r_h are computed by Eqs. (6) and (7), with the uncertainty of Eq. (13); (vi) the ringdown signals are fitted with sums of damped sinusoids and compared with the quasinormal-mode frequencies predicted from the measured flow [8, 12, 30]. All scripts will be released with the data (Sect. 3.12).

3.10 The dual-capsule (BEF-2026/M) apparatus

Stage 1 concerns the optional installation of the He II module inside the inner capsule of the author's dual-capsule apparatus, whose concept is described in [16] and whose current configuration ("BEF-2026/M", unpublished design documents of the author) is summarised here only to the extent needed to specify the interfaces of the helium module; its physics claims are not part of this paper. The apparatus consists of three nested capsules (Fig. 5a): an outermost "extra" capsule of ≈30 m inner diameter, an outer capsule of ≈18 m inner diameter, and a stationary inner capsule shaped as a vertical prolate ellipsoid 12 m from pole to pole. The inner-capsule wall is layered (90 cm SiC–SiC composite, 90 cm tungsten–steel, 100 cm lead, 30 cm circulating water); its interior is at 1 atm of air and houses, in the upper compartment, a live test subject (a 9 kg pig in a protective suit) for a 24 h run, and two 2 T superconducting pole magnets at the top (N) and bottom (S) of the cavity. In the gap between the inner and outer capsules two relativistic energy shells are generated: a 50 MV electron arc between rotating tungsten–rhenium pole electrodes (electron Lorentz factor $\gamma_e = 98.8$) and a ring-laser shell; two 10 T toroidal superconducting rings above and below the outer capsule provide the guide field. The /M variant additionally carries nano-gap Casimir panels and an interferometric mirror layer, neither of which interacts with the helium module. The whole assembly is sited in a sealed underground cavern.

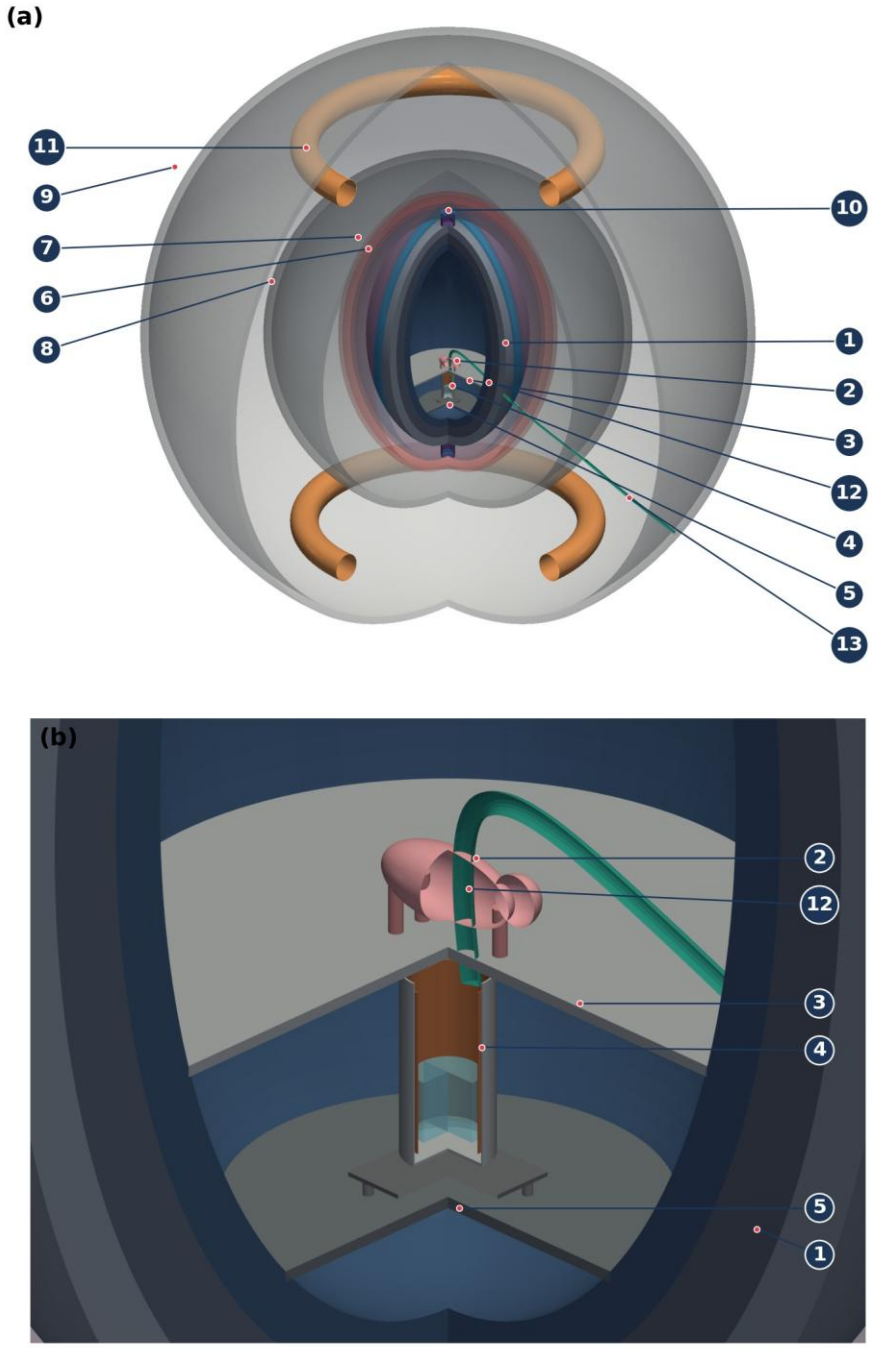


Fig. 5 (Color online) Optional integration of the He II module into the inner capsule of the dual-capsule apparatus (Stage 1), isometric three-dimensional quarter section; capsule and shell proportions are schematic, the cryostat module is drawn to scale. (a) Three capsules, two energy shells, pole electrodes and toroidal magnets. (b) Enlargement of the lower compartment of the inner capsule. Numbered parts: 1 inner-capsule wall (layered SiC–SiC / tungsten–steel / lead / water); 2 live-subject compartment (1 atm air, pig); 3 gas-tight partition floor between subject and cryogenic compartments; 4 He II vortex cryostat module (Figs. 1, 2 and 4, true size); 5 vibration-isolation platform; 6 first energy shell (electron arc); 7 second energy shell (ring laser); 8 outer capsule; 9 extra (outermost) capsule; 10 tungsten–rhenium pole electrodes (top/bottom); 11 toroidal superconducting magnets (top/bottom); 12 cryogenic feed and vapour-return lines through the inner-capsule wall; 13 shielded service conduit through the gap and the outer sphere to the external gas-handling plant

3.11 Integration of the helium module (Stage 1)

The complete Stage 0 cryostat (0.62 m × 1.3 m) is installed on its isolation platform in the lower compartment of the inner capsule, on the axis, below a gas-tight partition floor (Fig. 5b, parts 3–5); the compartment is ≈4 m in diameter and ≈1.8 m tall. A liquid at 1.6 K cannot share a volume with a living subject in 1 atm of air, so the separation is mandatory, and the cryogenic compartment carries its own oxygen monitors and is vented to the service conduit. Helium cannot be liquefied inside the capsule during a run; the module must therefore be connected to an external plant. Two options are specified (Fig. 3b and Table 1).

Option A, closed-loop recondensing circuit (baseline). The bath vapour is returned through a DN100 line of ≈15 m length, which passes through the inner-capsule wall (part 12), crosses the gap inside a water-cooled, lead-shielded service conduit that follows the mechanical support of the inner capsule (part 13), and exits through the outer sphere to a room-temperature pump, purifier and gas buffer outside the apparatus. The purified gas is returned at ≈20 bar to a two-stage pulse-tube cryocooler cold head (≈1.5 W at 4.2 K class) mounted next to the bath inside the module, where it is condensed at the 4 K stage and dripped back into the bath; the cryocooler compressor (7–9 kW, water cooled) also stays outside the outer sphere and is connected by flexible high-pressure lines through the same conduit. The viscous conductance of the 15 m return line is ≈3.1 m³/s, i.e. a pressure drop of only ≈1.3 Pa at the design throughput, so the line length is not a limitation. The circuit is closed and the helium inventory is conserved over the 24 h run; the cryocooler, however, is a vibration source and must be mounted on its own isolators with a flexible thermal link to the bath.

Option B, sealed autonomous module. If no line may cross the gap during a run, the module operates on its own liquid inventory: at the design heat load the 24 h boil-off is ≈576 g of helium (≈4.0 L of liquid, ≈3.2 m³ of gas at standard conditions), well within the 27 L available after pump-down, and the vapour is either compressed by a small oil-free diaphragm compressor into a ≈215 L buffer at 15 bar or adsorbed on an activated-charcoal sorption pump cooled by the 4 K stage; the capacity of such a pump must be measured, not assumed. Option B avoids all penetrations but gives up continuous pressure regulation and requires the pumping to 1.6 K to be completed before the capsule is sealed.

Three interface constraints follow from the apparatus itself. (i) Magnetic field: the lower pole magnet (2 T) is close to the module; helium-4 is unaffected, but the magnetically coupled drive, the camera and the electronics are not, so that for Stage 1 the propeller is replaced by a piezoelectrically driven bellows pump and all electronics are placed in a shielded enclosure

outside the strong-field region; ruthenium-oxide thermometers have a small, calibrated magnetoresistance. (ii) Radiation and heat: the 50 MV arc produces bremsstrahlung; the 3.1 m layered wall of the inner capsule is the only shielding, and the boil-off rate during ON periods is itself a measure of the additional heat load. (iii) Vibration: the rotating electrodes and the external plant are decoupled by the platform and the bellows sections as in Stage 0, and every run is vetoed by the accelerometer channels.

Table 1 Interface parameters of the He II module inside the inner capsule (Stage 1); design values, not measurements

Item	Value	Note
Location	lower compartment, on axis, below partition floor	≈4 m diameter, ≈1.8 m tall
Module envelope / mass	0.62 m × 1.3 m; ≈250 kg with platform	Stage 0 cryostat unchanged
Helium inventory	≈27 L He II after pump-down	≈29 m³ STP total
Design heat load	0.15 W at 1.6 K	boil-off 0.40 g/min
Option A: vapour-return line	DN100, ≈15 m, Δp ≈ 1.3 Pa	closed loop, cryocooler recondenser
Option A: cryocooler	2-stage pulse tube, ≈1.5 W at 4.2 K class	compressor 7–9 kW outside outer sphere
Option B: 24 h boil-off	≈576 g, ≈4.0 L liquid, ≈3.2 m³ STP	215 L buffer at 15 bar or sorption pump
Penetrations	2 × DN100 + electrical, through inner wall and outer sphere	water-cooled, lead-shielded conduit
Magnetic field at module	up to ≈2 T (lower pole magnet)	non-magnetic bellows drive; shielded electronics
Radiation	bremsstrahlung from 50 MV arc	3.1 m layered wall; boil-off monitored
Run duration	24 h	matches subject run
Safety	O_2 monitors, relief valves, gas-tight partition	cryogenic compartment vented to conduit

3.12 Calculation model and use of AI tools

All numbers in this paper are produced by an open Python calculation model (calc.py, results.json) and checked by an independent script (verify.py) that recomputes every quantity from the primary constants; the figure scripts read the same results file. In accordance with the journal's policy, the author declares that large-language-model tools were used for the literature search, for checking the calculations and for page layout; they were not used to generate scientific claims, data or figures of results, and the author takes full responsibility for the content.

4 Measurement method and protocol

4.1 Mapping $\gamma_{eff}(r)$ by Doppler separation

Because the dispersion is flat near $\lambda*$, the laboratory-frame phase speeds of waves travelling with and against the flow simply add and subtract:

$$c_{\pm} = c_w \pm v_\theta, \quad v_\theta = (c_+ - c_-)/2, \quad c_w = (c_+ + c_-)/2 \tag{12}$$

The same procedure in the radial direction gives v_r, and at each radius $\gamma_{eff} = [1 - (v_\theta^2 + v_r^2)/c_w^2]^{-1/2}$. Error propagation gives

$$\delta\gamma/\gamma = \beta\,\gamma^2\,\delta\beta \tag{13}$$

With v and c each measured to 1 %, $\delta\gamma/\gamma \approx 0.47$ % at $\beta = 0.5$. As $\beta \to 1$ the γ^2 term makes the uncertainty grow rapidly, so the ergoregion boundary is additionally determined directly: the radius at which counter-propagating azimuthal waves are brought to rest in the laboratory is $C/c_w \approx 6.42$ mm, and adding the measured radial component gives $r_e = 6.70$ mm.

4.2 Bound states and ringdown

A vortex excited by a short wave packet performs damped oscillations analogous to the quasinormal modes of black holes, as observed in a water vortex [7] and in superfluid helium [9, 11]. The frequencies and damping times are compared with the values computed from the measured velocity profile [8, 12]; this comparison is an independent check of the $\gamma_{eff}(r)$ map.

4.3 Protocol

1. **Cool-down:** the bath is filled at 4.2 K and pumped to ≈1.6 K; the λ transition is confirmed by the thermometers and by the jump in the vapour-pressure–heat-input relation.
2. **Static calibration:** with the propeller off, the wave generator is scanned from 10 to 100 Hz and the dispersion curve is measured; c_w and $\lambda*$ are determined experimentally (expected ≈9.89 cm/s and ≈3.13 mm at $T \to 0$ values, ≈9.72 cm/s and ≈3.03 mm at 1.6 K).
3. **Vortex formation:** the propeller speed is increased in steps; the side camera records the threshold at which the surface dimple becomes a hollow core; the circulation is obtained from the velocity profile as $\Gamma = 2\pi\, r\, v_\theta$.
4. **Mapping:** Doppler separation is performed for r = 1–30 mm; $\gamma_{eff}(r)$, r_e and r_h are obtained.
5. **Ringdown:** wave-packet excitation; frequencies and damping of the damped oscillations are measured.

6. **Parity and repeatability:** all measurements are repeated with the propeller rotation reversed (Sect. 7).

7. **Control records:** accelerometers, microphone, bath pressure, level and temperature are recorded synchronously throughout every run.

5 Calculated results

Table 2 collects the He II properties, the design values and the calculated quantities; Table 3 gives the radial profile of the effective Lorentz factor for surface waves.

Table 2 Properties of He II, design values and calculated quantities ($T \to 0$ surface tension; see Sect. 2.4 for the 1.6 K values)

Quantity	Value	Source / equation
Density ρ ($\approx$1.6 K)	$\approx$145 kg/m³	[18]
Surface tension σ ($T \to 0$)	$\approx 3.54\times10^{-4}$ N/m	[20, 18]
First-sound velocity c_1	$\approx$237 m/s	[18]
Landau critical velocity v_L	58.8 m/s	Eq. (3)
$\gamma_{eff,max}$ for bulk sound	1.032	Eq. (3)
Minimum surface-wave speed c_w	9.89 cm/s	Eq. (4)
Measurement wavelength λ_* / frequency f_*	3.13 mm / 31.6 Hz	Eq. (4)
Circulation quantum κ	9.97×10^{-8} m²/s	h/m_4
Design number of quanta N	4×10^4	design
Minimum N ($r_e \geq \lambda_*$)	1.87×10^4	Eq. (9)
Ergoregion radius r_e	6.70 mm	Eq. (6)
Analogue-horizon radius r_h	1.92 mm	Eq. (6), D/C = 0.3
Hollow-core radius	0.75 mm	Eq. (8)
Surface depression at r_e	0.50 mm	$c_w^2/2g$
Flow speed at the core edge	0.89 m/s ($\ll v_L$)	$\sqrt{(2gh_0)}$
Ideal drain flow rate	$\approx$48 mL/s	$2\pi D h_0$
Φ/c^2 of the helium mass in the cell	1.4×10^{-27}	$GM/(R c^2)$
Design heat load / boil-off	0.15 W / 0.40 g/min	Eq. (14)
Required pumping speed at 7.5 mbar	$\approx$19 m³/h	Sect. 3.4

Table 3 Radial profile of the effective Lorentz factor for surface waves (Eq. 7)

Radius	Absolute value (mm)	γ_{eff}
1.05 r_e	7.03	3.28
1.25 r_e	8.37	1.67
1.50 r_e	10.05	1.34
2.00 r_e	13.40	1.15

Radius	Absolute value (mm)	γ_{eff}
3.00 r_e	20.09	1.06
5.00 r_e	33.49	1.02
r_e (ergoregion boundary)	6.70	$\rightarrow \infty$

Figure 6 summarises the calculations. Panel (a) shows that bulk sound is confined to $\gamma_{eff} \leq 1.032$ by the Landau limit, whereas surface waves reach the whole range. In panel (b) the flow speed decreases as 1/r and crosses the surface-wave speed at $r_e = 6.70$ mm, where γ_{eff} diverges. Panel (c) gives the free-surface profile to scale: outside the ergoregion the surface is almost flat (the depression at r_e is only 0.50 mm), the funnel deepens towards the core and reaches the floor at 0.75 mm. Panel (d) shows why the measurement wavelength is chosen at $\lambda* \approx 3.13$ mm.

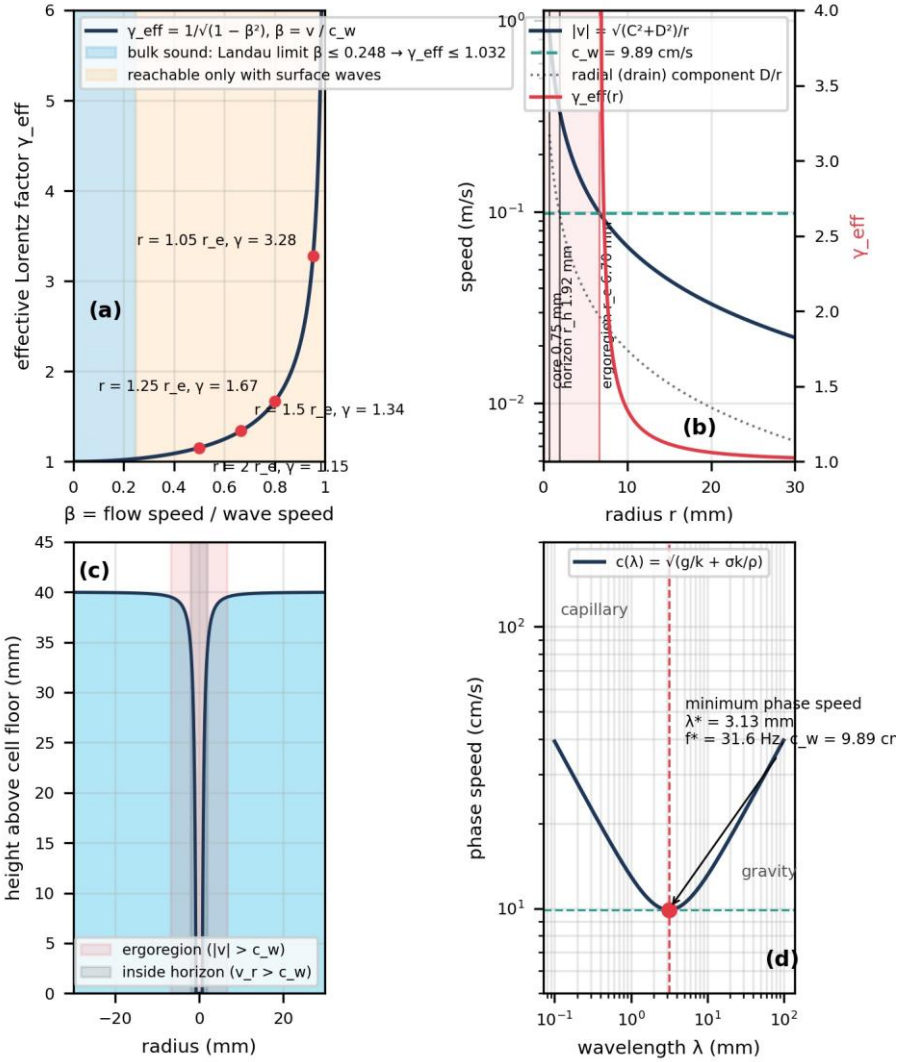


Fig. 6 (Color online) Calculated quantities. (a) Effective Lorentz factor versus β and the ranges accessible to bulk sound (Landau limit) and to surface waves. (b) Vortex velocity profile, radial component and $\gamma_{eff}(r)$; the vertical lines mark the core, the analogue horizon and the ergoregion. (c) Free-surface profile to scale. (d) Dispersion of He II surface waves and the chosen measurement point

6 Expected outcome of Stage 1 in the dual framing

The energy shells of the apparatus do not act directly on the effective metric in the helium: helium-4 is neutral and its magnetic interaction is very weak, so the effective metric is fixed by the helium flow alone. The only question that Stage 1 can ask is therefore: does the wave speed or the ringdown frequency in the helium change while the shells are ON?

Standard general relativity ($\xi = 1$). By the equivalence principle, wave and ringdown frequencies measured with a local clock inside the capsule do not change at all, because the clock and the helium slow down together in the same potential. Measured against a reference clock outside the capsule, the shift is at most the shell potential $|\Phi_s/c^2|$, which is $\approx 3.8\times10^{-47}$ for the two-shell 50 MV design (BEF-2026/M) and $\approx 8.3\times10^{-39}$ for the stored-E-layer design R2 [16]. No measurable difference is expected.

BEF hypothesis ($\xi \gg 1$). The effect scales as $\xi|\Phi_s/c^2|$. If the ringdown frequency is measured against the external reference to $\approx 10^{-3}$, a null result gives $\xi < 2.6\times10^{43}$ (BEF-2026/M) or $\xi < 1.2\times10^{35}$ (R2). These bounds are far weaker than the $\approx 10^{18}$–10^{28} bounds obtained with optical and nuclear clocks in the author's earlier work [16].

Table 4 summarises the ON/OFF expectation for the two apparatus designs.

Table 4 ON/OFF expectation for Stage 1 (ringdown-frequency precision 10^{-3} assumed)

Apparatus design	$\lvert\Phi_s/c^2\rvert$ (GR, $\xi = 1$)	Expected difference (GR)	ξ bound with He II
BEF-2026/M (two shells, 50 MV)	3.8×10^{-47}	not measurable	$< 2.6\times10^{43}$
BEF-2026-R2 (stored E-layer)	8.3×10^{-39}	not measurable	$< 1.2\times10^{35}$

Recommendation. Stage 1 adds no meaningful sensitivity to the ξ test. Stage 0 should therefore be carried out first in an independent low-temperature laboratory; Stage 1 should be considered only if Stage 0 succeeds, and only as a second demonstration channel.

7 Systematic errors and a warning from the literature

The risk of spurious signals in rotating cryogenic systems is well documented. Tajmar et al. reported anomalous signals in mechanically independent gyroscopes above rings spinning at low temperature [31] and subsequently performed similar measurements close to rotating liquid helium [32]. An independent measurement by Graham et al. with a lead disc and a ring-laser gyroscope was consistent with zero within 1σ [33], and Tajmar later measured signals about two orders of magnitude smaller with a modified set-up, attributing the earlier anomalies most

probably to acoustic vibration [34]. The following precautions are taken here: sensors are placed outside the cryostat on a separate isolation platform; every measurement is repeated for both rotation senses; pressure fluctuations from helium evaporation are recorded; and, if Stage 1 is performed, the ON/OFF labels are kept blind until the analysis is complete.

8 Relation to the black-hole-matter hypothesis

Volovik [35] showed that the low-energy excitations of superfluid helium-3 behave like an effective spacetime metric, gauge fields and particles. This is the best-established counterpart in the literature of proposition Ö1 of the author's hypothesis [17], that the excitations of a single condensed substance appear as "particles". The proposed experiment is a concrete laboratory demonstration of this idea: the flow of a single quantum liquid produces, for its own waves, a geometry with a horizon.

As shown in Sect. 2.7, the node-spacing function $n_e(r)$ of the Börekci-2 metric is the inverse of the effective Lorentz factor of the Schwarzschild river. This equality is a known property of the Painlevé–Gullstrand form; the contribution here is to interpret it in the "node compression" language of the hypothesis and to connect it with the "flow" language of analogue gravity. An honest limit must be stated: analogue experiments mimic how waves propagate in a curved geometry (kinematics), not how geometry arises from matter through Einstein's equations (dynamics) [3]. The experiment therefore supports that spacetime *can* be a medium; it does not prove that spacetime *is* a medium made of black-hole matter.

9 Discussion and limitations

- **Circulation target.** The design requires $N = 4\times10^4$ quanta; the minimum is $\approx1.87\times10^4$. Švančara et al. [9] reported "thousands" of quanta; the September 2026 preprint of the same group [14] reports about 1.2×10^5 quanta contributing to the central vortex of a draining flow above a 10 mm orifice, part of which is distributed around the hollow core. The design target therefore appears reachable, but the preprint has not yet been peer-reviewed and the quanta actually concentrated in the giant core must be measured. Should only $N = 10^4$ be reached, $r_e \approx 1.67$ mm, smaller than $\lambda*$, the waves cannot resolve the ergoregion, and reliable measurement is limited to $r \geq \lambda*$, where $\gamma_{eff} \approx 1.18$.
- **Idealisation.** The draining-vortex model is two-dimensional; the real flow is three-dimensional with a vertical component near the drain [23, 24]. The velocity profile must therefore be measured, not assumed.

- **Dispersion.** The effective metric is well defined only near $\lambda*$; at shorter and longer wavelengths the results require dispersion corrections [30].
- **Damping.** At 1.6 K the normal-fluid fraction damps the surface waves; lower temperature reduces the damping at the cost of pumping capacity (Sect. 3.4).
- **Surface tension.** The 6 % spread between published values of σ [20, 22] and its temperature dependence (Sect. 2.4) change c_w by at most 2 % and are absorbed by the static calibration.
- **Scope.** This is a design proposal; all numbers are calculated predictions and none is presented as measured data.

10 Conclusion

Superfluid helium-4 is the most suitable natural medium known for producing an effective Lorentz factor. With bulk sound this factor reaches at most 1.032. With surface waves an ergoregion and an analogue horizon can be produced, and γ_{eff} grows without bound as the ergoregion boundary is approached. The proposed Stage 0 apparatus, specified here down to its helium supply, purification, pumping and recovery circuit, its flow loop and its metrology, can measure the $\gamma_{eff}(r)$ map, the analogue horizon and the ringdown at laboratory scale and independently of the dual-capsule apparatus. The effective factor applies only to waves in the helium and produces no real time dilation for clocks or a living subject. Integration into the inner capsule is possible with either a closed-loop recondensing circuit or a sealed autonomous module, but it adds no meaningful sensitivity to the ξ test, so the independent pre-experiment is recommended first. The relation between the node-spacing function of the Börekci-2 metric and the effective Lorentz factor of the river model (Eq. 11) is the interpretation of a known mathematical identity in the language of the hypothesis and can be used to connect the hypothesis with the analogue-gravity literature.

Statements and Declarations

Funding. The author received no specific grant or financial support from any organisation for the submitted work; the work was carried out with the author's own means.

Competing interests. The author is the applicant of Turkish patent application TÜRKPATENT 2026/011037 concerning the dual-capsule (BEF) apparatus described in Sect. 3.10. The Stage 0 part of this work is independent of that application. The author has no other financial or non-financial interests to disclose.

Author contributions. Hasan Börekci conceived the study, designed the apparatus, performed the calculations and wrote the manuscript.

Data and code availability. No experimental data were generated. The calculation model (calc.py), the independent verification script (verify.py), the results file (results.json) and the figure scripts are available from the author on request and will be deposited in a public repository upon acceptance.

Ethics approval and consent. Not applicable: no experiments involving humans or animals were performed. The live subject mentioned in Sect. 3.10 belongs to the separately described dual-capsule programme and is not part of the present work.

Related work by the author. The dual-capsule apparatus and the phenomenological parameter ξ are described in a preprint [16]; the black-hole-matter hypothesis and the Börekci-2 metric in a preprint [17] currently under consideration elsewhere. The present paper does not re-use text from those works; it specifies a new, independent experiment.

References

1. W.G. Unruh, Phys. Rev. Lett. 46, 1351 (1981). https://doi.org/10.1103/PhysRevLett.46.1351
2. M. Visser, Class. Quantum Gravity 15, 1767 (1998). https://doi.org/10.1088/0264-9381/15/6/024
3. C. Barceló, S. Liberati, M. Visser, Living Rev. Relativ. 14, 3 (2011). https://doi.org/10.12942/lrr-2011-3
4. J. Steinhauer, Nat. Phys. 12, 959 (2016). https://doi.org/10.1038/nphys3863
5. J.R. Muñoz de Nova, K. Golubkov, V.I. Kolobov, J. Steinhauer, Nature 569, 688 (2019). https://doi.org/10.1038/s41586-019-1241-0
6. T. Torres, S. Patrick, A. Coutant, M. Richartz, E.W. Tedford, S. Weinfurtner, Nat. Phys. 13, 833 (2017). https://doi.org/10.1038/nphys4151
7. T. Torres, S. Patrick, M. Richartz, S. Weinfurtner, Phys. Rev. Lett. 125, 011301 (2020). https://doi.org/10.1103/PhysRevLett.125.011301
8. T. Torres, S. Patrick, M. Richartz, S. Weinfurtner, Class. Quantum Gravity 36, 194002 (2019). https://doi.org/10.1088/1361-6382/ab3d48
9. P. Švančara, P. Smaniotto, L. Solidoro, J.F. MacDonald, S. Patrick, R. Gregory, C.F. Barenghi, S. Weinfurtner, Nature 628, 66 (2024). https://doi.org/10.1038/s41586-024-07176-8
10. S. Grebenev, J.P. Toennies, A.F. Vilesov, Science 279, 2083 (1998). https://doi.org/10.1126/science.279.5359.2083
11. P. Smaniotto, L. Solidoro, P. Švančara, S. Patrick, M. Richartz, C.F. Barenghi, R. Gregory, S. Weinfurtner, Black-hole spectroscopy from a giant quantum vortex, arXiv:2502.11209 (2025, v3 2026). https://doi.org/10.48550/arXiv.2502.11209
12. L. Solidoro, S. Patrick, S. Weinfurtner, R. Gregory, Phys. Rev. Lett. 135, 051401 (2025). https://doi.org/10.1103/7kjp-vrml

13. V.S. Barroso, P. Švančara, C. Goodwin, S.C. Ajithkumar, I. Dimina, S. Schiattarella, P. Smaniotto, L. Solidoro, M. Cromb, R. Prizia, A.J. Kent, S. Weinfurtner, Phys. Rev. Appl. 26, 014080 (2026). https://doi.org/10.1103/dh9b-k6hm

14. P. Švančara, L. Solidoro, P. Smaniotto, S. Patrick, S. Schiattarella, M.T. Jarema, S.M.D. Gregory, V.S. Barroso, M. Richartz, A. Avgoustidis, C.F. Barenghi, R. Gregory, S. Weinfurtner, End state of the experimental black-hole bomb, arXiv:2609.05595 (2026). https://doi.org/10.48550/arXiv.2609.05595

15. M. Desrochers, D.J.J. Marchand, P.C.E. Stamp, Proc. Natl. Acad. Sci. U.S.A. 122, e2421273122 (2025). https://doi.org/10.1073/pnas.2421273122

16. H. Börekci, A near-light-speed enclosing energy field as a positron source and candidate time-dilation capsule, Research Square preprint (2026). https://doi.org/10.21203/rs.3.rs-9999735/v1

17. H. Börekci, A black-hole-matter hypothesis for spacetime geometry, energy and particles: the Börekci-2 node-spacing metric, literature basis and experimental constraints, Zenodo preprint (2026). https://doi.org/10.5281/zenodo.22932796

18. R.J. Donnelly, C.F. Barenghi, J. Phys. Chem. Ref. Data 27, 1217 (1998). https://doi.org/10.1063/1.556028

19. D.R. Allum, P.V.E. McClintock, A. Phillips, R.M. Bowley, Philos. Trans. R. Soc. A 284, 179 (1977). https://doi.org/10.1098/rsta.1977.0008

20. M. Iino, M. Suzuki, A.J. Ikushima, J. Low Temp. Phys. 61, 155 (1985). https://doi.org/10.1007/BF00682735

21. R. Schützhold, W.G. Unruh, Phys. Rev. D 66, 044019 (2002). https://doi.org/10.1103/PhysRevD.66.044019

22. P. Roche, G. Deville, N.J. Appleyard, F.I.B. Williams, J. Low Temp. Phys. 106, 565 (1997). https://doi.org/10.1007/BF02395922

23. S. Inui, T. Nakagawa, M. Tsubota, Phys. Rev. B 102, 224511 (2020). https://doi.org/10.1103/PhysRevB.102.224511

24. W. Ruffenach, L. Galantucci, C.F. Barenghi, J. Low Temp. Phys. 212, 375 (2023). https://doi.org/10.1007/s10909-023-02943-9

25. H. Yano, K. Ohyama, K. Obara, O. Ishikawa, J. Phys.: Conf. Ser. 969, 012002 (2018). https://doi.org/10.1088/1742-6596/969/1/012002

26. A.J.S. Hamilton, J.P. Lisle, Am. J. Phys. 76, 519 (2008). https://doi.org/10.1119/1.2830526

27. F. Pobell, Matter and Methods at Low Temperatures, 3rd edn. (Springer, Berlin, 2007). https://doi.org/10.1007/978-3-540-46360-3

28. M. Takeda, K. Mutoh, Appl. Opt. 22, 3977 (1983). https://doi.org/10.1364/AO.22.003977

29. S. Wildeman, Exp. Fluids 59, 97 (2018). https://doi.org/10.1007/s00348-018-2553-9

30. S. Patrick, S. Weinfurtner, Phys. Rev. D 102, 084041 (2020). https://doi.org/10.1103/PhysRevD.102.084041

31. M. Tajmar, F. Plesescu, B. Seifert, J. Phys.: Conf. Ser. 150, 032101 (2009). https://doi.org/10.1088/1742-6596/150/3/032101

32. M. Tajmar, F. Plesescu, AIP Conf. Proc. 1208, 220 (2010). https://doi.org/10.1063/1.3326250

33. R.D. Graham, R.B. Hurst, R.J. Thirkettle, C.H. Rowe, P.H. Butler, Physica C 468, 383 (2008). https://doi.org/10.1016/j.physc.2007.11.011

637 34. M. Tajmar, Supercond. Sci. Technol. 24, 125011 (2011). https://doi.org/10.1088/0953-
638 2048/24/12/125011

639 35. G.E. Volovik, The Universe in a Helium Droplet (Oxford University Press, Oxford, 2003; paperback
640 2009). https://doi.org/10.1093/acprof:oso/9780199564842.001.0001

Supplementary Files

This is a list of supplementary files associated with this preprint. Click to download.

- ESM1.zip